



Swansea University  
Prifysgol Abertawe



## Cronfa - Swansea University Open Access Repository

---

This is an author produced version of a paper published in:

*Journal of The Electrochemical Society*

Cronfa URL for this paper:

<http://cronfa.swan.ac.uk/Record/cronfa50771>

---

### **Paper:**

Wint, N., Barrett, Z., Williams, G. & McMurray, H. (2019). The Study of AA2024 De-Alloying Using Luminol Electrogenerated Chemiluminescence Imaging. *Journal of The Electrochemical Society*, 166(11), C3417-C3430.  
<http://dx.doi.org/10.1149/2.0481911jes>

---

This item is brought to you by Swansea University. Any person downloading material is agreeing to abide by the terms of the repository licence. Copies of full text items may be used or reproduced in any format or medium, without prior permission for personal research or study, educational or non-commercial purposes only. The copyright for any work remains with the original author unless otherwise specified. The full-text must not be sold in any format or medium without the formal permission of the copyright holder.

Permission for multiple reproductions should be obtained from the original author.

Authors are personally responsible for adhering to copyright and publisher restrictions when uploading content to the repository.

<http://www.swansea.ac.uk/library/researchsupport/ris-support/>



## The Study of AA2024 De-Alloying Using Luminol Electrogenerated Chemiluminescence Imaging

N. Wint,<sup>1</sup>\*,<sup>z</sup> Z. S. Barrett, G. Williams, and H. N. McMurray\*

Materials Research Center, College of Engineering, Swansea University, Bay Campus, Crymlyn Burrow, Swansea SA1 8EN, United Kingdom

This paper describes the use of luminol electrogenerated chemiluminescence (ECL) to image the re-distribution of electrochemically active copper (copper in electrical contact with the substrate) at the surface of AA2024-T351 corroding in NaCl electrolyte. AA2024 samples are thermo-mechanically treated to produce a macroscopically inhomogeneous distribution of intermetallic particles. The AA2024-T351 samples are allowed to corrode by immersion in 0.51 M aqueous NaCl and (ex-situ) ECL measurements are performed to follow copper re-distribution. Luminol ECL light emission is orders of magnitude more intense on copper than aluminum and macro and microscopic images are obtained to elucidate the re-distribution of electrochemically active copper. S phase de-alloying produces a radical re-distribution of copper on a microstructural scale (1-10 μm) but macroscopic copper distributions (1-10 mm) remain largely unchanged. In-situ experiments using the SVET show that macroscopic copper distribution directs localization of corrosive attack such that net anodic activity (pitting/intergranular attack) is concentrated in regions with lowest surface coverage of copper and net cathodic activity is concentrated in regions of highest coverage. Results are explained in terms of the role of solution chemistry and pH in influencing the transition from transient to stable pitting.

© The Author(s) 2019. Published by ECS. This is an open access article distributed under the terms of the Creative Commons Attribution 4.0 License (CC BY, <http://creativecommons.org/licenses/by/4.0/>), which permits unrestricted reuse of the work in any medium, provided the original work is properly cited. [DOI: 10.1149/2.0481911jes]



Manuscript submitted March 25, 2019; revised manuscript received June 6, 2019. Published June 19, 2019. This was Paper 877 presented at the Cancun, Mexico, Meeting of the Society, October 29–November 3, 2006. *This paper is part of the JES Focus Issue on Advanced Techniques in Corrosion Science in Memory of Hugh Isaacs.*

The de-alloying of Cu containing phases and precipitates, and facile oxygen reduction kinetics on the elemental Cu so produced, are known to be important factors promoting the chloride-induced corrosion of AA2024-T3.<sup>1</sup> Furthermore, it has been shown that the re-deposition of separated Cu particles, and the re-plating of Cu<sup>2+</sup> cations, can profoundly influence the overall rate and distribution of the cathodic oxygen reduction reaction (ORR).<sup>1</sup> The present paper is intended to discover two things: 1) how the distribution of Cu influences the localization of corrosive attack on the alloy surface and 2) how that corrosive attack influences the corrosion-driven re-distribution of Cu. It may be understood that, taken together, these two phenomena describe the dynamic interplay between Cu (re)distribution and localized corrosion on AA2024. In order to carry out such a study, two methodologies are required. The first (based on SVET) is used to characterize the time-dependent evolution of localized corrosion current distribution and the second (based on luminol ECL) is used to characterize the time-dependent (re)distribution of electrochemically active Cu. Electrochemically active Cu is metallic (or intermetallic) Cu which is electrically connected to the alloy substrate and therefore capable of contributing to the distribution of local corrosion current by supporting interfacial electron transfer processes, specifically those associated with the ORR. This is in contradistinction to electrochemically inactive Cu which is either present as a non-metallic corrosion product or metallic particles electrically isolated within a corrosion product layer.

AA2024-T3 is a commercially important wrought alloy used throughout the aerospace industry due to its high strength to weight ratio, and suitability for age hardening.<sup>2</sup> The alloy's mechanical strength is derived from the addition of Cu alloying elements (~5 wt%),<sup>3</sup> which results in the formation of secondary phase intermetallic particles (IMPs) within the alloy matrix. Despite its desirable mechanical properties, the corrosion resistance of AA2024-T3 generally decreases with increased Cu content, this being attributed to the enhanced electrocatalytic activity for the cathodic ORR exhibited by Cu rich particles and regions within the matrix.<sup>4-10</sup> It is the galvanic coupling of the IMPs, to the matrix, which makes AA2024-T3 highly susceptible to localized corrosion,<sup>11,12</sup> particularly in chloride rich environments

where pitting corrosion, intergranular corrosion, and stress corrosion cracking of the alloy have all been observed.<sup>1,13-16</sup>

The galvanic relationships between the IMPs commonly found within AA2024-T3, and the surrounding matrix, have been characterized extensively elsewhere.<sup>17,18</sup> Initially, Al<sub>2</sub>CuMg (S phase) IMPs are anodic with respect to the surrounding, Al oxide covered, matrix.<sup>4</sup> In comparison, Al<sub>6</sub>Mn<sup>19</sup> Al<sub>2</sub>Cu (θ)<sup>20</sup> and Al<sub>3</sub>Fe<sup>21</sup> become the site of the ORR (the relevant cathodic reaction in near neutral electrolytes) due to their relative nobility with respect to the Al matrix.<sup>8</sup> However, these findings are further complicated by the re-distribution of Cu on the alloy surface, which in turn produces large localized changes in electrocatalytic activity with respect to the cathodic ORR.<sup>1,22,23</sup>

The two primary sources of re-distributed Cu are the S phase particles (~50 wt% Cu), which account for 60% of the IMPs present on the AA2024-T3 surface,<sup>1</sup> and the matrix.<sup>24</sup> The initial dissolution of Mg in the S phase particles inhibits its re-passivation and allows the dissolution of Al. This leaves a mechanically unstable,<sup>22</sup> high surface area porous Cu 'sponge'<sup>23</sup> and it has been reported that 10–100 nm Cu clusters detach from the alloy surface and can be carried away by corrosion product or moving solution.<sup>1</sup> Based on these findings it is plausible that non-faradaic release and movement of Cu occurs, but the extent to which this contributes to Cu enrichment is, as yet, unknown.<sup>23</sup>

Following liberation, Cu is able to adopt its free corrosion potential and undergo oxidation within the electrolyte,<sup>23</sup> and the presence of Cu<sup>2+</sup> ions in the electrolyte in which AA2024 is immersed has been demonstrated previously using Pt and Ag rotating ring disk electrodes.<sup>12,21,22</sup> Re-plating of the ions may then occur at flaws in the AA2024 oxide layer which is, itself, semiconducting.<sup>25</sup>

The production of OH<sup>-</sup> ions via the ORR causes an increase in local pH. This increased alkalinity activates the matrix Al, which then undergoes dissolution via Equation 1.<sup>22,24-27</sup>



Dissolution of the matrix, which contains 0.2-0.5 wt% Cu in solid solution,<sup>25</sup> can expose significant quantities of Cu held in solid solution, which can then agglomerate into Cu particles. De-alloying will also allow the exposure of Cu containing dispersoids, GP phases and new, intact IMPs which can then become cathodes. Previous studies have reported enhanced ORR currents for solution annealed and

\*Electrochemical Society Member.

<sup>z</sup>E-mail: [n.wint@swansea.ac.uk](mailto:n.wint@swansea.ac.uk)

quenched samples in which matrix Cu would be enriched.<sup>24</sup> They concluded that although Cu enrichment is expected to occur as a result of alkaline Al dissolution, the resultant anodic current contribution would tend to consume the cathodic current contribution and therefore Cu enrichment due to matrix dissolution only makes a limited contribution to maintenance of anodic sites.<sup>24</sup>

A number of studies have concentrated on investigating the role that alloy microstructure plays in determining the location of localized corrosion, (such as pitting corrosion), and the establishment of stable pits on AA2024 has been shown to occur immediately adjacent to S phase particles.<sup>4,28,29</sup> It has also been proposed that the alkalinity developed at the cathodic IMPs can dissolve the adjacent matrix giving rise to the appearance of grooves and pit-like clusters<sup>1,7,28-31</sup> which could later switch to an acidic pitting mechanism.<sup>7</sup>

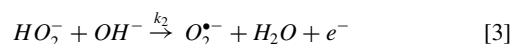
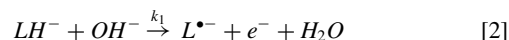
It is therefore clear that the susceptibility of AA2024-T3 to localized corrosion, such as pitting, is a consequence of both its composition and microstructural features, most notably the IMPs.<sup>29</sup> It is likely that pit initiation occurs either through selective dissolution (in the case of S phase particles) or through cathodically mediated peripheral pitting of the matrix (in the case of de-alloyed S phase particles and cathodic Al-Cu-Fe-Mn particles). However, these transient pits are more numerous and smaller than the stable, acid filled pits observed on heavily corroded AA2024-T3. A question therefore exists as to whether alloy microstructure and distribution of IMPs can influence the transition from transient, to stable, pitting and thereby determine the location and number density of stable pits.

The first aim of the current paper is to determine how the initial surface concentration of Cu-rich IMPs influences the probability of stable pit formation. That is to establish, unequivocally, whether or not the highest number concentration of stable corrosion pits coincides with the highest surface concentration of Cu-rich IMPs. The second aim is to dynamically follow the corrosion driven re-distribution of electrochemically active Cu. The third aim is to determine whether or not Cu re-distribution produces any time-dependent change or evolution in the localization of corrosive attack.

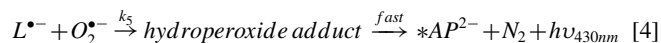
To achieve the above, a thermomechanical treatment is applied to AA2024 to control the macroscopic distribution of Cu based IMPs over a length scale which allows variations in local current density (which result from local variations in surface coverage of electrochemically active Cu) to be resolved by the scanning vibrating electrode technique (SVET). The ability of SRET (a precursor of SVET), to study the pitting corrosion of AA2024-T4 in chloride solutions, has been demonstrated previously.<sup>32</sup> Electrogenerated chemiluminescence (ECL) imaging is also used to both monitor de-alloying, and the subsequent re-distribution, of electrochemically active Cu (which evolves dynamically as a result of the corrosion process), and deter-

mine whether the predominant source of re-distributed Cu is the S phase (Al<sub>2</sub>CuMg) particles, or Cu held in solid solution (or as dispersoids and GP zones) in the matrix. Finally, the current distribution (as determined by SVET) is correlated with both the initial distribution of IMPs and the (re)distribution of electrochemically active Cu, to determine whether re-distribution of Cu appreciably effects the time-dependent distribution of current or localization of corrosive attack.

ECL imaging exploits the well-known electrochemical oxidation of luminol (3-aminophthalhydrazide) in aqueous alkaline solution.<sup>33-35</sup> Oxidation of the luminol monoanion (LH<sup>-</sup>) occurs via Equation 2 (shown in Figure 1) and is initiated by an external voltage (anodic polarization) which is applied to the working electrode.<sup>36,37</sup> The product of Equation 2 is the luminol L<sup>•-</sup> radical anion.<sup>34</sup> The simultaneous oxidation of hydrogen peroxide to form the superoxide radical anion O<sub>2</sub><sup>•-</sup> occurs via Equation 3.



Luminol ECL imaging uses the light which is emitted when the hydroperoxide adduct decomposes to produce aminophthalate in its excited state (\*AP<sup>2-</sup>) via Equation 4. This reaction takes place homogeneously within the bulk electrolyte proximal to the electrode surface and the relaxation of the molecule releases energy in the form of light with a wavelength ( $\nu$ ) of ~450 nm.<sup>37</sup> The first acid dissociation coefficient (pK<sub>a1</sub>) associated with the hydrolysis of the hydroperoxide adduct is 10.4<sup>37</sup> and it has been shown that only the monoanionic form decomposes to generate aminophthalate in its excited state.<sup>34</sup>



Equation 4 is, in part, dependent upon the chemical composition (and electrocatalytic behavior with respect to LH<sup>-</sup> oxidation) of the working electrode and it is therefore apparent that ECL emission is dependent upon both mass transport (of luminol or H<sub>2</sub>O<sub>2</sub> to the electrode surface) and kinetic effects.<sup>34,38</sup> Different electrode materials can vary greatly in their efficiency for producing ECL light emission. Here we show that Cu is orders of magnitude more efficient than Al in this respect. It is this finding which makes the ECL imaging of electrochemical active Cu possible.

Under quiescent (unstirred) electrolyte conditions the emission of ECL may conveniently be initiated by applying an anodic going potential pulse (Figure 2).<sup>38,39</sup> The value of the potential required to induce the oxidation of LH<sup>-</sup> via Equation 2 is highly dependent upon electrode material.<sup>34,35,38</sup> However, electrolyte pH, and both LH<sup>-</sup> and

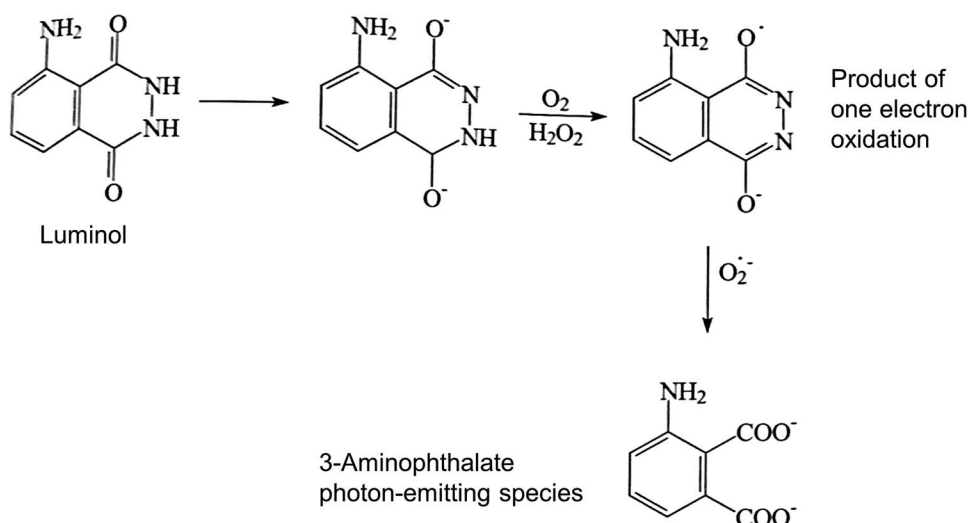
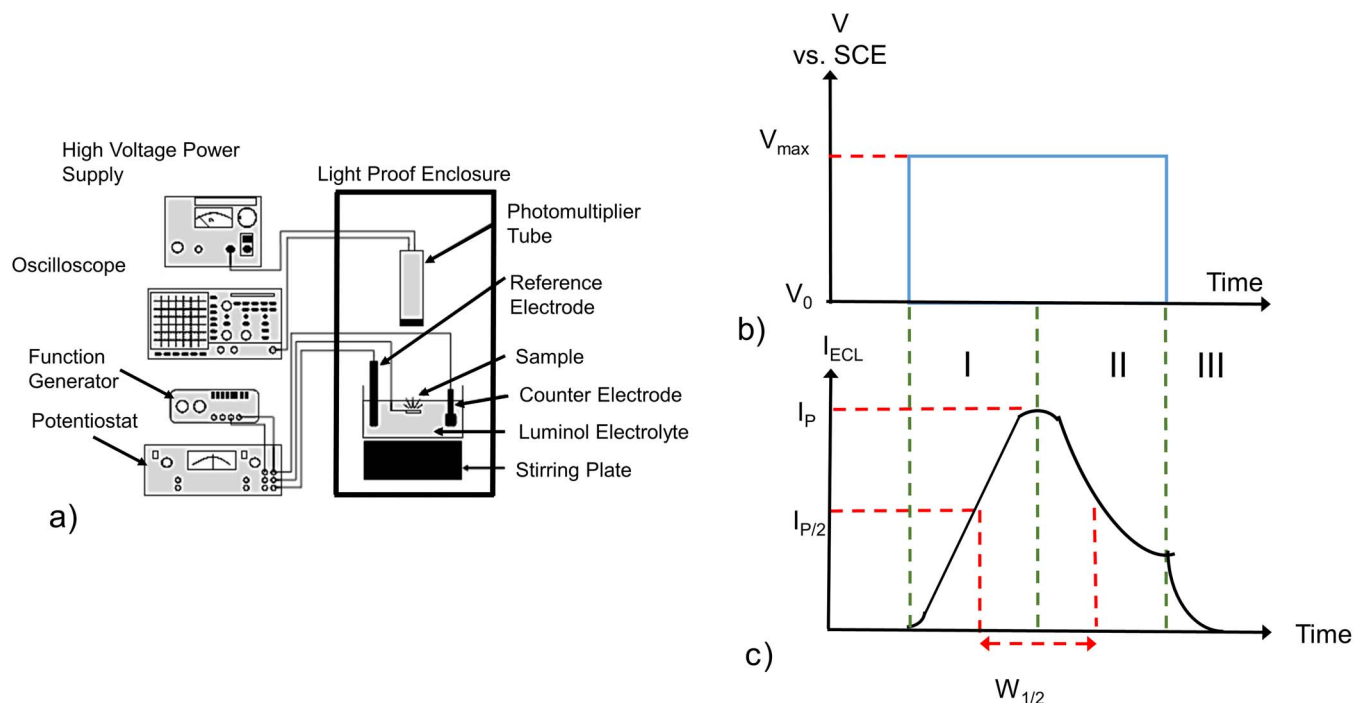


Figure 1. Reaction scheme for the oxidation of luminol.



**Figure 2.** a.) Schematic of the apparatus used during time dependent electrogenerated chemiluminescent emission studies and b.) Applied square wave pulse and c.) typical ECL waveform where  $I_p$  is the maximum ECL intensity,  $W_{1/2}$  is the half width (width at half height),  $V_0$  is the starting potential of the applied pulse (0V vs. SHE) and  $V_{max}$  is the maximum potential of the applied pulse.

$H_2O_2$  concentrations<sup>35,38–41</sup> also play a role in the resulting waveform of ECL emission intensity with respect to time. The contrast achievable in luminol ECL imaging is limited by background light emission from a chemiluminescent (CL) reaction occurring between luminol and  $H_2O_2$  in bulk electrolyte.<sup>42,43</sup> This homogeneous CL process is catalyzed by transition metal ions in solution and has previously been exploited as a means of detecting trace quantities of transition metals.<sup>44,45</sup> Here we show that the background CL process can be effectively suppressed by addition of ethylenediaminetetraacetic acid (EDTA) to the experimental electrolyte. ECL efficiency is substantially unaffected by EDTA and ECL imaging contrast can therefore be maximized.

Luminol ECL differs from the ex-situ high vacuum techniques such as SEM, EDX and SIMS, which have previously been used to study Cu re-distribution on the surface of AA2024<sup>1,23,46–48</sup> in that it specifically, and selectively, images electrochemically active Cu. Furthermore, it permits the rapid imaging of Cu distribution over microscopic ( $\mu\text{m}$ ) and macroscopic (mm) length scales under electrolyte immersion conditions.

### Experimental

**Materials.**—Samples of pure metals were obtained in sheet form from Advent Research Materials. Al was of 99.999% purity and 1.2 mm thick whilst the 99.997% purity Cu sheet was 1.0 mm thick.

Cube shaped samples were cut from a 2.5 cm thick section of hot rolled plate AA2024-T351 produced by BAE Systems. The nominal alloying element concentrations for AA2024 are 0.5 wt% Si, 0.5 wt% Fe, 3.8–4.9 wt% Cu, 0.3–0.9 wt% Mn, 1.2–1.8 wt% Mg, 0.1 wt% Cr, 0.25 wt% Zn.<sup>1</sup> The alloy plate had undergone a thermo-mechanical process which resulted in a macroscopic inhomogeneous distribution of secondary phase particles in the matrix (Figure 3).

**Methods.**—*Materials characterization.*—A cube shaped sample was removed from the AA2024-T351 plate. Experiments were conducted on the cube face which corresponded to the cross section of the plate (Figure 3). The cube sample face was ground to P1200 finish

using SiC abrasive paper and polished to a 2  $\mu\text{m}$  finish using diamond paste, before examination using a Phillips FEI XL30 CP electron microscope in backscatter mode. Electron backscatter images of the surface were taken at 0.5 mm intervals across the cube face. The contrast of the backscatter unit was increased such that the Cu rich area appeared bright white against a black matrix. Graftek Optilab Pro 6.2 was used to calculate the percentage of precipitate present in any image.

**SVET.**—Information regarding the apparatus, and calibration procedure used to obtain values of current flux density along the axis of probe vibration ( $j_z$ ) from the SVET voltage signal, are given elsewhere.<sup>49–54</sup> In brief, a 125  $\mu\text{m}$  diameter platinum micro tip, encased in glass (total diameter 250  $\mu\text{m}$ ), vibrated by an electromagnetic driver at a fixed frequency (140 Hz) and amplitude (25  $\mu\text{m}$ ) in the  $z$  direction. The SVET voltage signal is detected using a Perkin Elmer 7265 lock-in amplifier.

In the case that an electrolyte of conductivity  $K$  is used, the peak-to-peak SVET voltage signal  $V_{pp}$  is related to current flux density along the axis of probe vibration normal to the sample surface ( $j_z$ ) by Ohm's Law,  $V_{pp} = j_z (a_{pp}/K)$ . The quantity  $a_{pp}/K$  may then be defined as the SVET calibration factor and is measured galvanostatically, within the electrolyte of interest, using a specially devised two-compartment cell.<sup>49–53</sup> The calibration factor is obtained from the subsequent plots and allows the conversion of SVET  $V_{pp}$  signals to normal current density ( $j_z$ ) values.

Following calibration, the samples were securely fastened to the electrolyte tank and immersed in electrolyte. Scanning took place immediately after immersion and at 4 hour intervals over a total experimental time period of 24 hours thereafter. The scan height was 100  $\mu\text{m}$  above the sample. The dissolved oxygen concentration in bulk solution was assumed to be  $2.8 \times 10^{-4}$  M, the equilibrium concentration for air saturated water<sup>55</sup> and a temperature of 25°C was maintained throughout.

SVET is only able to detect localized corrosion currents, which arise in the case that anode-cathode spacing is greater than the scan height (in this case 100  $\mu\text{m}$ ), with any great efficiency. In the case that the spacing is  $< 100 \mu\text{m}$ , the current flux lines will not cross the scan

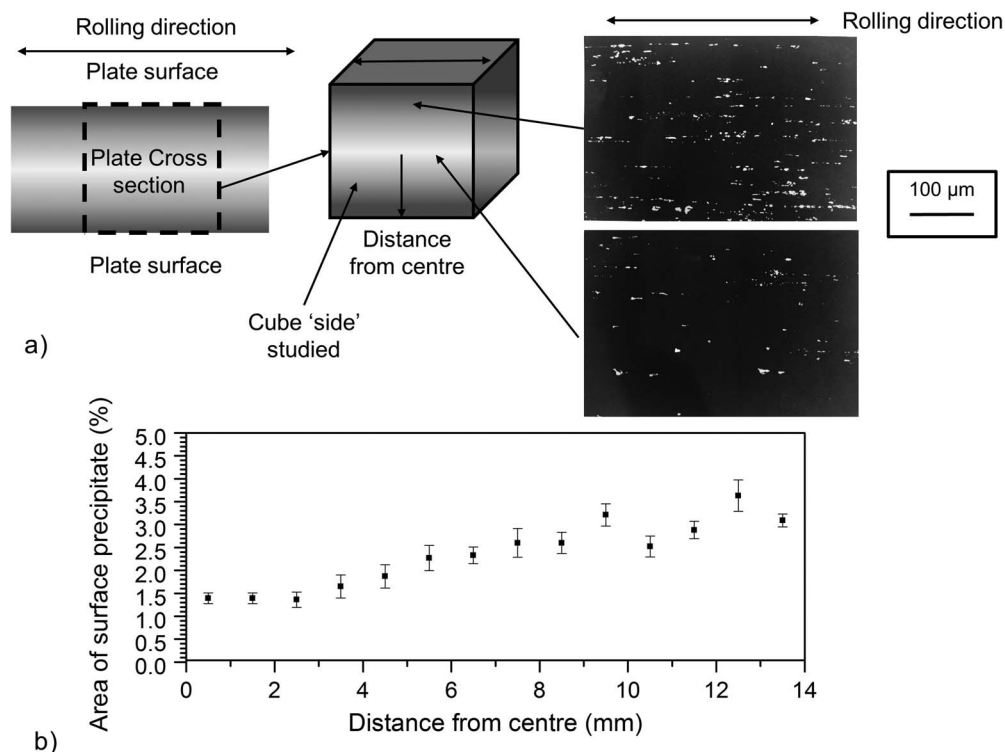


**Figure 3.** a.) Backscatter images showing distribution of Cu-rich particles at the edges and center of the cube face and b.) the variation in Cu rich particle concentration as a function of distance across the cube face. Error bars show one standard deviation.

plane, and thus not be detected, or at best with low efficiency.<sup>49,53</sup> For a point current source the theoretical width at half maximum ( $whm$ ) of the SVET response peak is  $1.53z$  (where  $z$  is the probe height).<sup>54</sup> The finite width of the electrically sensitive portion of the SVET tip also means that peak broadening can occur. The  $whm$  for the SVET used here has previously been given as  $\sim 260 \mu\text{m}$  in the case that  $z = 100 \mu\text{m}$ .<sup>52</sup>

**ECL studies.**—A solution of 0.1 M aqueous  $\text{Na}_2\text{CO}_3$  acted as both supporting electrolyte and pH buffer for luminol ECL. The solution pH was adjusted to pH 12 by adding equi-molar solutions of NaOH whilst dissolving in  $2.25 \times 10^{-3}$  M luminol. This pH value was selected for two reasons; firstly, the value of the first acid dissociation coefficient ( $\text{p}K_{a1}$ ) associated with the hydrolysis of the hydroperoxide adduct is 10.4.<sup>35,37</sup> Secondly, a decrease in  $I_p$  at  $\text{pH} > 12$  is predicted to occur as a result of the known decrease in aminothalate luminescence quantum yields at high pH.<sup>36</sup> EDTA was included in the electrolyte to complex trace transition metals in solution and so suppress homogeneous, background CL processes. Any required concentration of EDTA was achieved by volumetric additions of 0.1–0.001 M aqueous tetrasodium EDTA to the luminol solution.<sup>56,57</sup> A concentration of  $8 \times 10^{-3}$  M  $\text{H}_2\text{O}_2$  was similarly established by volumetric additions of aqueous  $\text{H}_2\text{O}_2$ . This concentration of  $\text{H}_2\text{O}_2$  is similar to values reported during similar work and was found empirically to produce optimal ECL light intensity.<sup>40,56,58–60</sup> All solutions containing  $\text{H}_2\text{O}_2$  were used within 12 hours of preparation.

**Time dependent ECL Intensity Studies.** Metal coupons of 20 mm  $\times$  15 mm were cut from various sheet materials. Electrical connection to each coupon was made via a multi strand wire. The wire was soldered to Cu samples. In the case of Al samples, a crimping process was used. A 10 mm  $\times$  10 mm area square of the metal coupon was masked off using tape and the rest of the sample coated in epoxy resin. Once the epoxy resin had set the tape was removed to expose a 100 mm<sup>2</sup> portion of the metal surface as the working electrode. The whole coupon was then epoxied to a glass holder to support it beneath the photomultiplier (PM) tube. Prior to each ECL experiment the working electrode surface

was ground to a P1200 finish using abrasive SiC paper and rinsed using distilled water.

Time dependent ECL intensity studies were conducted to investigate 1.) the relative efficiency of various metal surfaces in producing ECL and 2.) the extent to which the background CL process can be suppressed by adding EDTA to complex transition metal ions in solution, without suppressing the ECL process.

Measurements of time-dependent ECL intensity were made using the equipment shown in Figure 2a. A photomultiplier (PM) was used to detect the photons of light generated at the working electrode. The peak of spectral response of the Electron Tubes 9125A PM used here coincided with the maximum wavelength of light emitted by Equation 4 (450 nm).<sup>37</sup> This ensured that an adequate signal to noise ratio was achieved at lower light levels. An Electron Tubes PM28B bench top power supply was used to operate the tube at a voltage of 460 V, which ensured that the maximum safe anode current of the tube (100  $\mu\text{A}$ ) was not exceeded. An Electron Tubes A1 transimpedance amplifier was used to convert the PM current to a voltage, which was recorded by a digital storage oscilloscope (Tektronix TDS340A). The square wave potential pulse (Figure 2b) required to initiate ECL was generated using a Topward 8201 pulse generator and applied to the working electrode using a Wenking LB75M potentiostat. A platinum gauze counter electrode and a saturated calomel reference electrode (SCE) were used in a standard 3 electrode cell arrangement. The electrochemical cell and PM tube were contained within a light tight chamber and a temperature of 25°C was maintained throughout.

**ECL imaging.**—Whilst the photomultiplier tube used during time dependent studies gives quantitative data regarding the intensity of ECL emission, it does not provide any spatial information. However, digital imaging of ECL emission allows light emitted at the working electrode to be spatially resolved. ECL images of the cube sample face were taken at regular intervals with the aim of mapping the distribution of electrochemically active Cu as de-alloying occurs. The apparatus used during ECL imaging is shown in Figure 4, and primarily consisted of a Hamamatsu C5985 low light video camera driven by

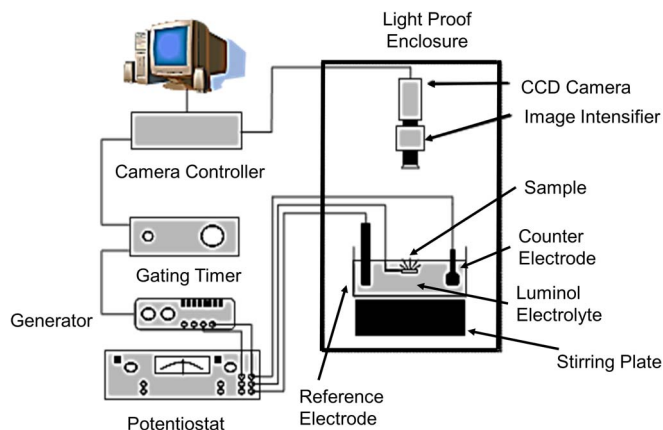


**Figure 4.** Schematic of the apparatus used during electrogenerated chemiluminescent imaging.

a Hamamatsu C5985 power supply. The charged couple device (CCD) image sensor was controlled using a Hamamatsu Argus 20 digital image processor, which allowed full control of all aspects of the CCD such as image integration time and image gain. The image processor allowed image manipulation such as background subtraction. The Argus 20 was controlled by Hamamatsu HPDCPx32 software installed on an IBM compatible PC and communication between the Argus 20 and PC was made by a SCSI interface. At low light levels a C2400-80 multi-channel plate intensifier was attached in front of the CCD to increase sensitivity. For the majority of imaging work an Edmund Optics close focus zoom lens was attached to the camera. An electronic timing circuit was used to ensure that digital image capture coincided with the application of the potential pulse to the working electrode.

**Lateral resolution of ECL imaging.**—ECL light emission occurs homogeneously in a reaction layer of solution near the working electrode surface. Consequently, the ability to resolve two adjacent ECL emitters (in this case portions of the working electrode which emit light by ECL at a greater or lesser intensity than the surrounding area) is determined by the reaction layer thickness. The reaction layer thickness ( $\mu$ ) refers to the distance between the electrode surface (where  $O_2^-$  and  $L^{\bullet-}$  are generated upon application of a potential pulse) and the point within the bulk electrolyte to which they have diffused before reacting to produce light via Equation 4. Under steady state conditions, decomposition of an electrochemically oxidized species O, which in this case is the hydrogen peroxide adduct, will follow Equation 5.

$$\frac{i}{n \cdot F \cdot A} = m_R [C_R^* - C_R(x=0)] = m_O C_O(x=0) + \mu k C_O(x=0) \quad [5]$$

where  $i$  is the current,  $n$  is the number of electrons,  $F$  is Faraday's constant,  $A$  is the electrode area,  $m_R$  is the mass transfer coefficient of the reduced species,  $C_R^*$  is the concentration of the reduced species in bulk solution,  $x$  is the distance from the electrode surface,  $m_O$  is the mass transfer coefficient of the oxidized species and  $C_O$  is the concentration of the oxidized species. Electrode surfaces at which Nernstian reactions occur are in equilibrium with  $C_R(x=0)$  and  $C_O(x=0)$ . Beyond  $\mu$  the intensity of ECL emission becomes negligibly small. In the case that the  $\mu >$  emitter active site for O production size, no size information will be obtained and individual emitters will not be resolved in the case that inter-emitter distance  $< \mu$ .

Given the small size (1-25  $\mu\text{m}$ ) of IMPs present within the AA2024-T3 system, a preliminary study was conducted to determine to what extent it was possible to resolve features of this size by ECL imaging. In principle, reaction layer thickness is calculable if all the relevant kinetic parameters are known. However, such a calculation is far from straightforward and it is easier simply to make an empirical estimate of reaction layer thickness by experiment.<sup>61</sup> In so doing a three electrode cell with a platinum microdisc working electrode was

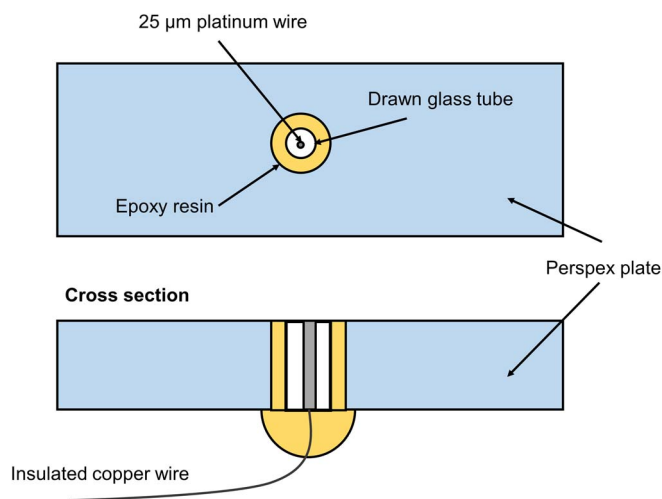


**Figure 5.** Schematic of the platinum microdisc working electrode used to determine the extent to which ECL is able to resolve IMPs.

utilized. The microdisc electrode was constructed by sealing a 10 mm long, 25  $\mu\text{m}$  diameter platinum wire in a glass tube and soldering a Cu wire to the free end. This assembly was then fixed into a hole in a Perspex plate using epoxy resin such that the end of the platinum wire was flush with the plate surface (Figure 5). The surface was polished to a 0.5  $\mu\text{m}$  finish using a diamond slurry. The CCD camera and image intensifier were attached to the camera port of a Meiji metallurgical light microscope. A glass dish, filled with luminol electrolyte, was mounted on the microscope stage and the electrode was immersed in the unstirred solution. A 45 second anodic pulse was applied and the emitted light was integrated on the camera CCD. The starting potential ( $V_0$ ) was 0 V vs. SCE and the maximum potential ( $V_{max}$ ) was 1 V vs. SCE. Images obtained were normalized by defining the lightest and darkest pixel within the image and distributing intermediate values proportionally between 0 (black) and 255 (white) using Adobe Photoshop.

**Corrosion and De-alloying of AA2024-T351.**—A 10 mm deep hole (1.5 mm diameter) was drilled into the face of the AA2024-T351 cube, opposite that which was to be studied. A multi-strand Cu wire was placed in the hole and fixed using fast set silver loaded epoxy resin. All remaining faces were insulated using PVC tape and epoxy resin. Samples were ground to a P1200 finish using SiC abrasive paper and polished to a 1  $\mu\text{m}$  finish using diamond paste. Following this they were de-greased and rinsed using acetone and distilled water. The cube was then immersed in 0.51 M NaCl to initiate corrosion and corrosion driven Cu re-distribution.<sup>13,22</sup> In other experiments, specifically intended to determine the effect of alkaline electrolyte pH on de-alloying of Cu present as a solid solution in the Al matrix, the cube sample face was immersed in 0.1 M  $\text{Na}_2\text{CO}_3$  at pH 12.<sup>13,24</sup> In both cases the cube face was allowed to adopt its free corrosion potential. All ECL imaging of the AA2024-T351 cube sample face was performed ex-situ. The sample was withdrawn from the corrosive electrolyte, rinsed with distilled water and immersed in luminol imaging electrolyte.

**ECL imaging of Cu distribution.**—A square wave potential pulse, from OCP to 0.8 V vs. SCE, was applied immediately following sample immersion. The pulse width (duration) was 1 second so that anodic damage to the material surface was minimized. All light emitted during this anodic pulse was integrated on the CCD of the low light camera.

The magnification necessary to image Cu re-distribution on a microstructural length scale was achieved using the same Meiji metallurgical microscope as described for the ECL reaction layer thickness measurements.

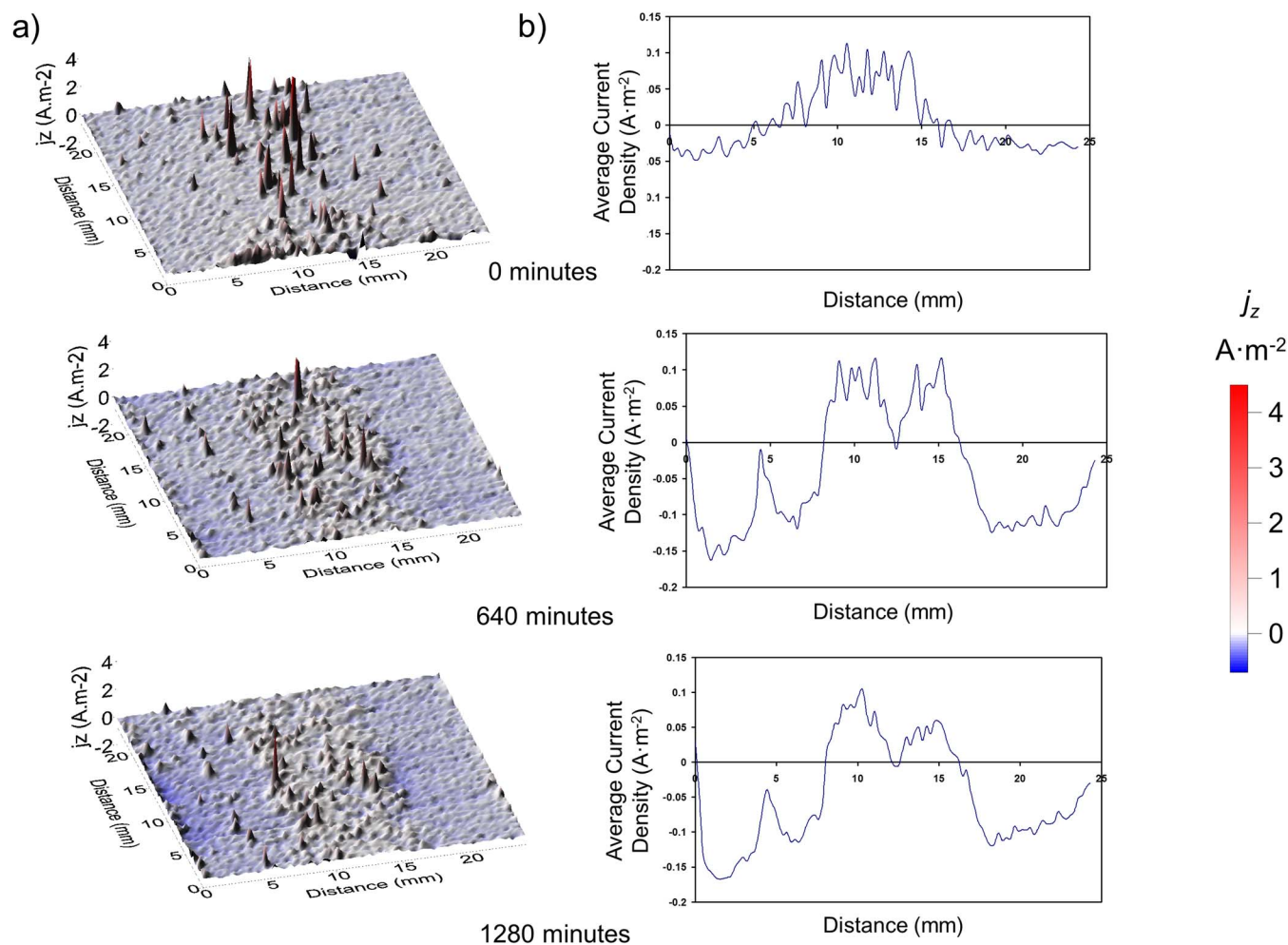


**Figure 6.** a.) SVET derived surface maps showing the distribution of normal current density  $j_z$  and b.) the corresponding time dependent distribution of  $j_z$  values along the  $x$  direction  $j_{z(x)}$ , obtained in the case that AA2024-T351 cube face is immersed in 0.51 M NaCl for various periods of time.

## Results

**SEM characterization.**—An in depth investigation into the microstructure and chemistry of AA2024-T3 has been completed previously and is beyond the scope of this paper.<sup>62</sup> However, it is clear from the backscatter images (where Cu rich IMPs appear light in color against the darker background of the Al matrix) shown in Figure 3, that surface coverage of IMPs [ $\text{Cu}_{\text{IMP}}$ ] is greatest at the edges of the cube sample face and is lower near the center. The images also demonstrate the elongation of precipitates along the rolling direction of the original AA2024 plate (Figure 3). The fractional surface coverage by Cu-rich IMPs (expressed as a percentage of total surface area) is plotted as a function of distance from the cube face center line in Figure 3b. The [ $\text{Cu}_{\text{IMP}}$ ] near the cube face edge is approximately twice that near the center line.<sup>62</sup>

**SVET determination of localized corrosion currents.**—Figure 6 shows a series of SVET derived  $j_{z(x,y)}$  area plots measured above the AA2024-T351 cube sample face freely corroding in 0.51 M aqueous NaCl at various times during sample immersion. It may be seen that corrosion remains highly localized throughout. Net anodic  $j_z$  (red) are discrete and take the form of symmetrical peaks with a  $whm$  of  $\sim 350$   $\mu\text{m}$ . SVET features are consistent with the presence of anodic corrosion pits acting as point current sources (that is to say the  $whm$  is close to the SVET instrumental  $whm$ <sup>36</sup> and the physical size of the pit opening cannot be determined by  $j_z$  data). These anodic  $j_{z(x,y)}$  peaks occur most frequently near the center line of the cube sample face.

Conversely, net cathodic  $j_z$  distributions are more continuous and net cathodic  $j_{z(x,y)}$  is concentrated toward the edges of the cube face.

The time dependent distribution of  $j_z$  values along the  $x$  direction in Figure 6a is perhaps shown more quantitatively in Figure 6b. To calculate the presented data,  $j_{z(x)}$  values were obtained using Equation 6

$$j_{z(x)} = \frac{1}{n} \sum_{y=0}^{y=n} j_{z(x, y)} \quad [6]$$

where  $n$  is the number of data point rows recorded by SVET along the  $y$  direction (100).

Figure 6 highlights two important trends. Firstly, the macroscopic distribution of  $j_z$  values (over a millimeter length scale) does not change appreciably with respect to time, that is to say that the cube face center is predominately anodic for the entire experimental period, whilst the edges remain cathodic. Secondly, the magnitude of  $j_{z(x)}$  appears to remain approximately constant throughout the 24 hour time period. At the end of the experimental period the sample was emersed, rinsed with distilled water and dried in air. It was imaged, photographically as seen in Figure 7. Figure 7 shows the sample surface to be heavily pitted, with dark corrosion pits occurring at the highest frequency near the sample center line. It also shows a darkening of the sample surface due to re-deposited Cu and Cu rich corrosion product. This darkening is most evident farthest from the sample center line. The anodic and cathodic current values shown in the SVET line integrals (Figure 6) are not well balanced. It is likely that the cathodic current values, which are substantially controlled by  $\text{O}_2$  transport, are overestimated due to the convection which occurs in the vicinity of the vibrating tip.<sup>63</sup>

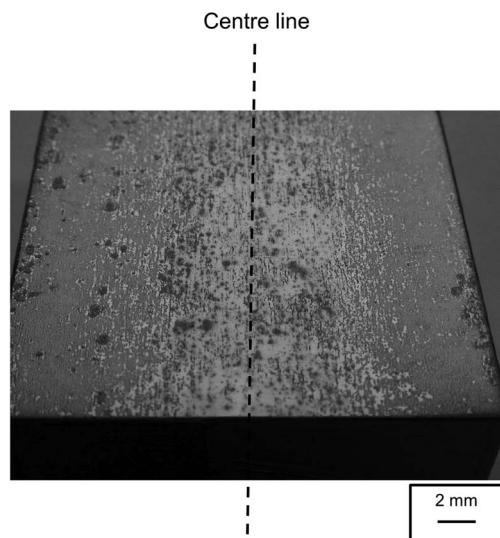


**Figure 7.** Image of the AA2024-T351 sample surface showing severe pitting within the central region following 24 hours immersion in 0.51 M NaCl.

**Time dependent ECL intensity.**—The voltage signal obtained from the PM tube/transimpedance amplifier apparatus was directly proportional to incident light intensity. Consequently, the relative ECL emission intensity could be recorded as a function of time by recording the voltage waveform. Figure 2 shows, schematically, b.) the anodic going square wave potential pulse applied to the working electrode and c.) the resulting ECL intensity waveform for a typical ECL experiment. Three distinct regions of the ECL waveform have previously been identified during an investigation into the kinetics of the luminol ECL reaction on a platinum electrode.<sup>38</sup> Region I (labelled on Figure 2) begins upon application of the square wave potential pulse and ends at the point at which the peak ECL intensity ( $I_p$ ) is reached. From this point (Region II) the light output falls as luminol is depleted at the electrode surface due to mass transport limitations. This decay continues until the applied pulse is removed. Upon removal of the applied potential the faradaic reaction ceases and light output falls following first order homogeneous kinetics (Region III).<sup>39</sup>

Figure 8 shows the form of the experimentally obtained ECL intensity-time response curves in the case that 1 second duration anodic pulses with various values of  $V_{max}$  are applied to a Cu electrode. The form of each  $I_{ECL}$  vs. time curve is similar to that observed previously for platinum.<sup>38</sup> Figure 8 shows that as  $V_{max}$  increases the peak value ( $I_p$ ) of  $I_{ECL}$  also increases. However, as  $V_{max}$  increases the dura-

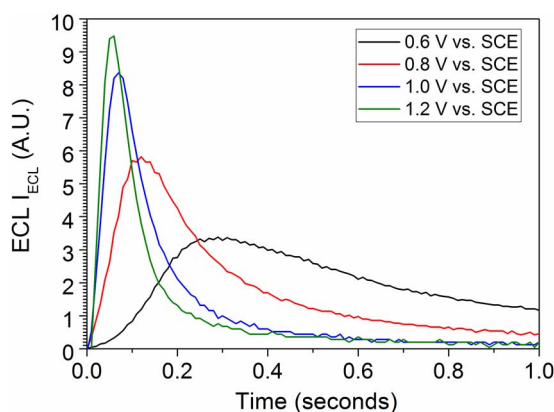


**Figure 8.** Typical ECL intensity response waveforms obtained following the application of a square wave potential pulse, of varying  $V_{max}$ , to a Cu electrode.

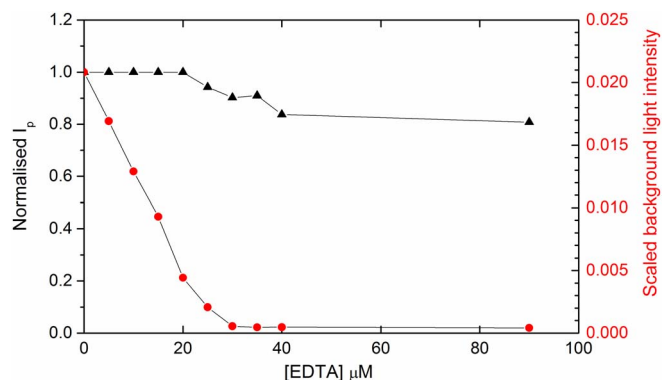


**Figure 9.** Effect of EDTA concentration on normalized ECL  $I_p$  values at an Cu electrode and background chemiluminescent light intensity scaled to maximum value of ECL  $I_p$ .

tion (width) of the  $I_{ECL}$  vs. time response decreases due to the more rapid depletion of luminol near the electrode surface.

**Effect of EDTA concentration.**—The Cu working electrode was subject to a square wave anodic potential pulse for which the start and final potential was 0 V vs SCE. The pulse potential amplitude  $V_{max}$  was 1.4 V vs. SCE and the pulse duration was 670 ms. The effect of [EDTA] on  $I_p$  is shown in Figure 9 for a pH 11.7 electrolyte containing  $3.5 \times 10^{-2}$  M  $H_2O_2$  and  $2.5 \times 10^{-3}$  M luminol. The  $I_p$  is reduced by around 20% as [EDTA] is increased from 0 to  $100 \times 10^{-6}$  M. A measure of the effect of [EDTA] on the background CL intensity of the electrolyte obtained in the absence of the working electrode is also shown. The background CL intensity is reduced by 98% when [EDTA] exceeds  $30 \times 10^{-6}$  M.

**ECL on Cu and Al.**—The effect of varying  $V_{max}$  on the intensity of ECL emission from pure Al and Cu was studied with the aim of optimising ECL image contrast for electrochemically active Cu distribution on Al. Figure 10 shows values of  $I_p$  on Cu and Al as a function of  $V_{max}$ . Figure 10 shows that ECL  $I_p$  values on Al are very low and change by less than an order of magnitude for  $V_{max}$  between 0 V vs. SCE and 1 V vs. SCE. By comparison ECL  $I_p$  values on Cu may be over three orders of magnitude greater than on Al and increase by three orders of magnitude when  $V_{max}$  is increased from 0 V vs. SCE to 1 V vs. SCE. On the basis of the findings in Figures 8 and 10, a  $V_{max}$  of 0.8 V vs. SCE was adopted as a convenient value to produce optimal sensitivity and contrast in the ECL imaging of Cu on Al.

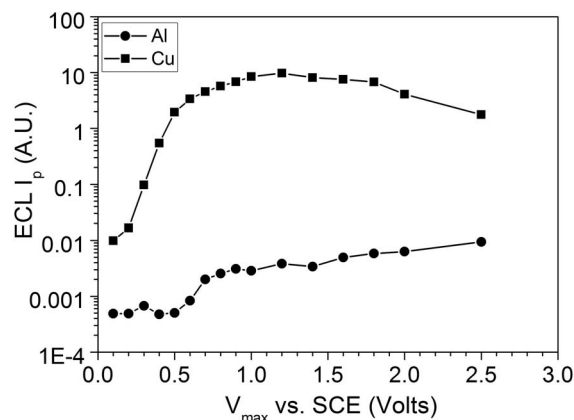


**Figure 10.** ECL  $I_p$  values for Cu and Al electrodes as a function of  $V_{max}$  when  $V_0 = 0$  V vs. SCE.

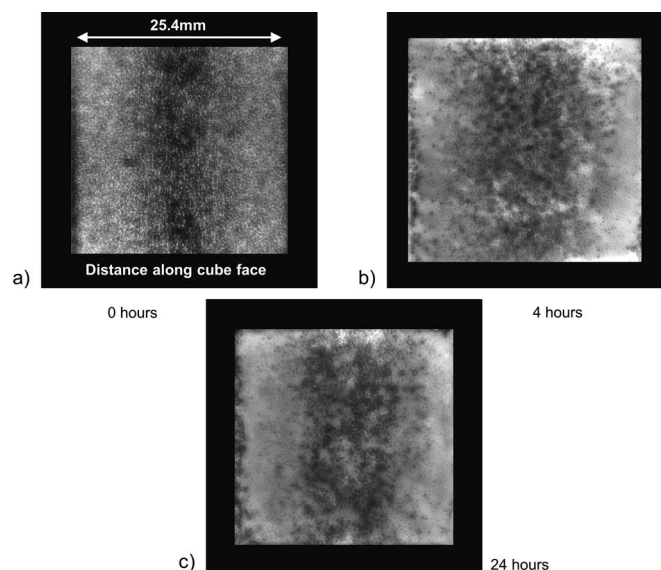


**Figure 11.** Normalized ECL images of AA2024-T351 after a.) 0 hours b.) 4 hours and c.) 24 hours of exposure to 0.51 M NaCl.

**Macro ECL imaging.**—The distribution of electrochemically active Cu on the surface of AA2024-T351 was established by ECL imaging un-corroded and (as an ex-situ measurement) corroded samples.

Figure 11a shows a macro (25 mm × 25 mm) ECL image of the un-corroded cube sample face. It is evident that the region of least intense ECL emission lies close to the center line of the sample. Furthermore, the pattern of ECL emission is characteristically speckled in nature. These two observations are consistent with ECL emission being associated with Cu-rich IMPs as shown in Figure 3. The sample could be subject to up to 5 imaging voltage pulses in the pH 12 ECL electrolyte before there was any detectable change in the appearance of the ECL image. On this basis, the ECL technique cannot be regarded as non-perturbing on AA2024-T351, however it can be regarded as minimally perturbing provided immersion in the ECL electrolyte is of short duration and imaging is performed using a single voltage pulse.

Re-polished cube face samples were allowed to corrode freely 0.51 mol.dm<sup>-3</sup> aqueous NaCl, for periods of 4 hours and 24 hours. At the end of these immersion times the samples were removed from the NaCl electrolyte, washed with distilled water and immersed in the luminol ECL electrolyte. The ECL images obtained after 4 hours and 24 hours of corrosion are shown in Figs. 11b and 11c, respectively. A comparison of Figures 11a, 11b and 11c shows that although the characteristic speckle pattern of ECL emission coarsens with corrosion time, the macroscopic distribution does not change significantly. This is perhaps better seen in Figure 12 which shows Figure 11 pixel values (averaged over 50 pixels in y direction) plotted as a function of distance along the x direction. The ECL intensity distribution on un-corroded and 24 hour corroded samples is broadly similar with minima on, or near, the mid line, and maxima near the sample edge. Given the minimally perturbing nature of ECL imaging any changes in electrochemically active Cu distribution implied by Figures 11a–11c may be ascribed to the effect of corrosion in the NaCl electrolyte.

Localized cathodic activity on AA2024-T351 will result in an increase in local electrolyte pH and a question arises as to whether the resulting activation and dissolution of the Al matrix might expose sub-surface Cu present either in solid solution or in the form of macro or microscopic precipitates. In an attempt to answer this question, de-alloying of the Al matrix was induced by immersing re-polished cube-face samples cube in pH 12 0.1 M Na<sub>2</sub>CO<sub>3</sub> for 4 hours. At this pH the anodic dissolution of Al is predicted to occur via Equation 1. Cu is predicted to be passive and therefore resistant to anodic dissolution even if electrically separated from the matrix. Similarly, the insolubility of Mg(OH)<sub>2</sub> at pH 12 will tend to disfavor S phase particle

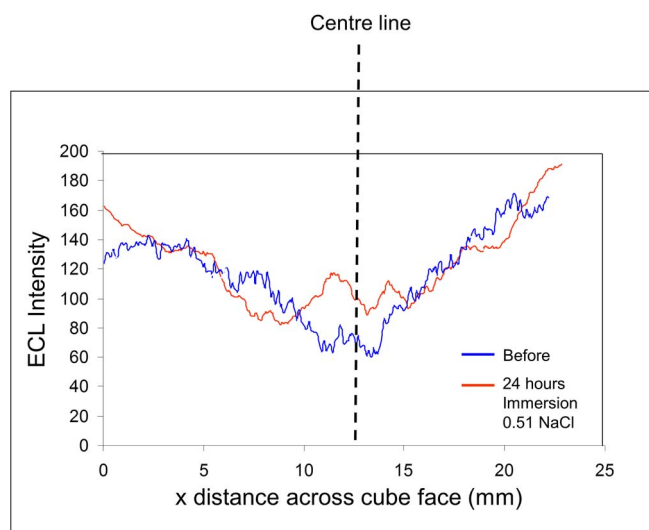


**Figure 12.** ECL image pixel value as a function of distance across the cube face prior to and post immersion in 0.51 M NaCl. An average pixel value was recorded for each 50 pixels in Figure 11 and measurements were made in 3 positions (3 different y values).

dissolution. Figure 13b shows the ECL emission pattern obtained at the end of the immersion period. A comparison of Figure 13b with the un-corroded ECL emission pattern indicates a re-distribution of light intensity away from the sample edge toward the center line. This is perhaps more clearly seen in Figure 14, which shows pixel value (averaged over 50 pixels in Figure 13) plotted as a function of distance across the cube face (x direction in Figure 13). Values were taken at three positions along the y axis (Figure 13) and the result averaged. The most probable source of the increased ECL light emission near the center line in Figures 13 and 14 is Cu which has been exposed following Al matrix dissolution.

**Micro ECL imaging.**—A question arises as to the dimensions of the ECL reaction layer thickness and the ability to laterally resolve physically small sources of ECL emission by optical imaging. In an attempt to answer this question, Figure 15a shows optical images of the immersed 25 μm platinum microdisc electrode under conditions of a.) illumination by an external light source and b.) ECL emission in the absence of any external light source (ECL imaging). The light intensity distribution (pixel values) along the axis X-X' in Figure 15a and Figure 15b were obtained using Sigma Scan Pro and are plotted in Figure 15c. The radial variation in light intensity across the microdisc surface probably results from a slight non-planarity in that surface producing a distortion of specular reflectance. Nevertheless, Figure 15c shows that the ECL intensity peak width is the same physical width of

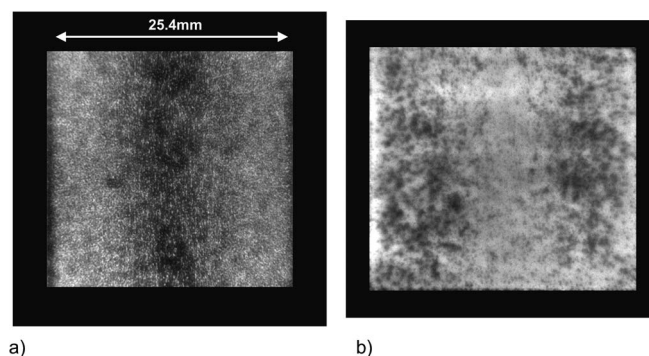


**Figure 13.** Normalized ECL images of AA2024-T351 after a.) 0 hours and b.) 4 hours exposure to pH 12 0.1 M Na<sub>2</sub>CO<sub>3</sub>.

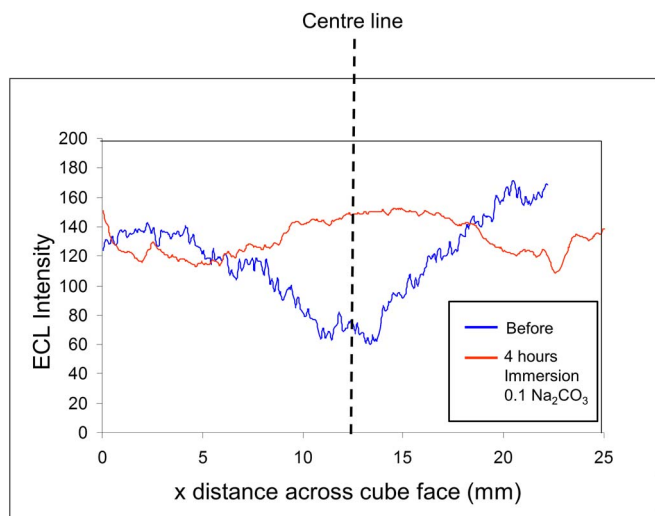


**Figure 14.** ECL image pixel value as a function of distance across the cube face prior to and post immersion in pH 12 0.1 M  $\text{Na}_2\text{CO}_3$ . An average pixel value was recorded for each 50 pixels in Figure 13 and measurements were made in 3 positions (3 different y values).

the microdisc give or take  $\sim 1 \mu\text{m}$ . This finding would suggest that the effective ECL reaction layer thickness  $< 1 \mu\text{m}$  and that ECL imaging by optical microscopy should be capable of laterally resolving two physically small ( $< 25 \mu\text{m}$ ) sources of ECL emission when these are separated by a distance  $\gg 2 \mu\text{m}$ .

Re-distribution of electrochemically active Cu over a microstructural length scale (1-100  $\mu\text{m}$ ) was followed using ECL imaging in conjunction with optical microscopy. Figure 16a shows images of a

small section near the center of the un-corroded cube face, obtained under reflected light. IMPs appear as dark spots against the bright matrix. The corresponding ECL image (Figure 16b) shows that areas of intense light emission coincide with the location of the IMPs. The variation in apparent intensity from particle to particle indicates that they differ in size and composition. Figure 16c shows a reflected light optical image of the same area after 4 hours immersion in  $0.51 \text{ mol}\cdot\text{dm}^{-3}$  NaCl. The dark spots associated with IMPs appear to be much greater in size, probably due to the presence of surrounding corrosion product and de-alloyed fragments of the original particles.<sup>1</sup> The corresponding ECL emission image (Figure 16d) shows limited number of bright spots corresponding to IMPs surrounded by a more general distribution of ECL light emission. After 24 hours corrosion in  $0.51 \text{ mol}\cdot\text{dm}^{-3}$  NaCl, the reflected light image of the sample surface (Figure 16e) again shows coarsening of the dark spots associated with IMPs. There is also some darkening of the surrounding matrix. However, the corresponding ECL image (Figure 16f) now exhibits a very different change in appearance. The original IMP centers appear dark and ECL activity is concentrated in halos around the original IMP positions. It would seem likely that these correspond to halos of electrochemically active Cu which has become re-distributed around the IMPs through a corrosion driven de-alloying process.<sup>1,12,22,23</sup>

An exactly similar procedure of imaging and corrosion was carried out for a small area near the edge of the cube face sample (an area of net cathodic activity in Figure 6). Figure 17a shows this area under reflected light. The IMPs again appear as dark spots against the bright matrix but at a significantly higher number density (per unit area) than in Figure 16a. The corresponding ECL image (Figure 17b) again shows that areas of intense ECL light emission coincide with the location of the IMPs in Figure 17a. Figure 17c shows a reflected light optical image of a similar area after corrosion by 4 hours immersion in  $0.51 \text{ mol}\cdot\text{dm}^{-3}$  aqueous NaCl. The dark spots associated with IMPs have increased in size but to a lesser extent than is the case in Figure 16c. The corresponding ECL image in Figure 17d shows a large

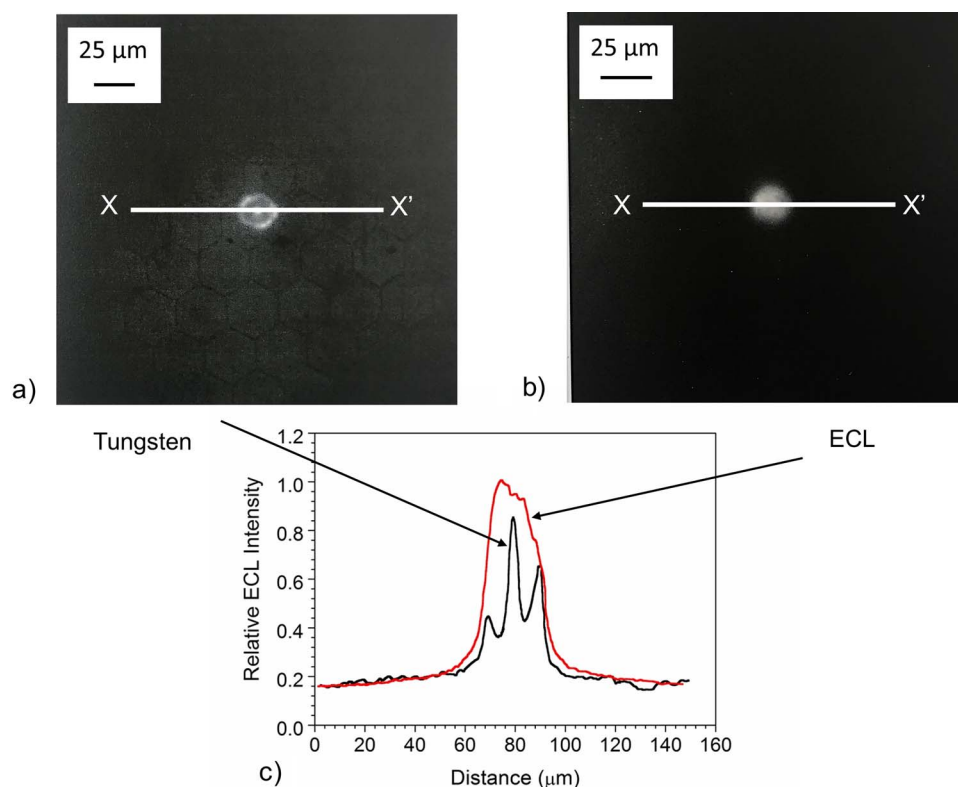


**Figure 15.** a.) Reflected light (tungsten illumination) image of a  $25 \mu\text{m}$  platinum wire electrode and b.) ECL emission image (obtained following the application of a 1 V vs. SCE potential pulse to the electrode for 45 seconds) and c.) the light intensity distribution (pixel values) along the axis X-X' in a.) and b.) obtained using Sigma Scan Pro.

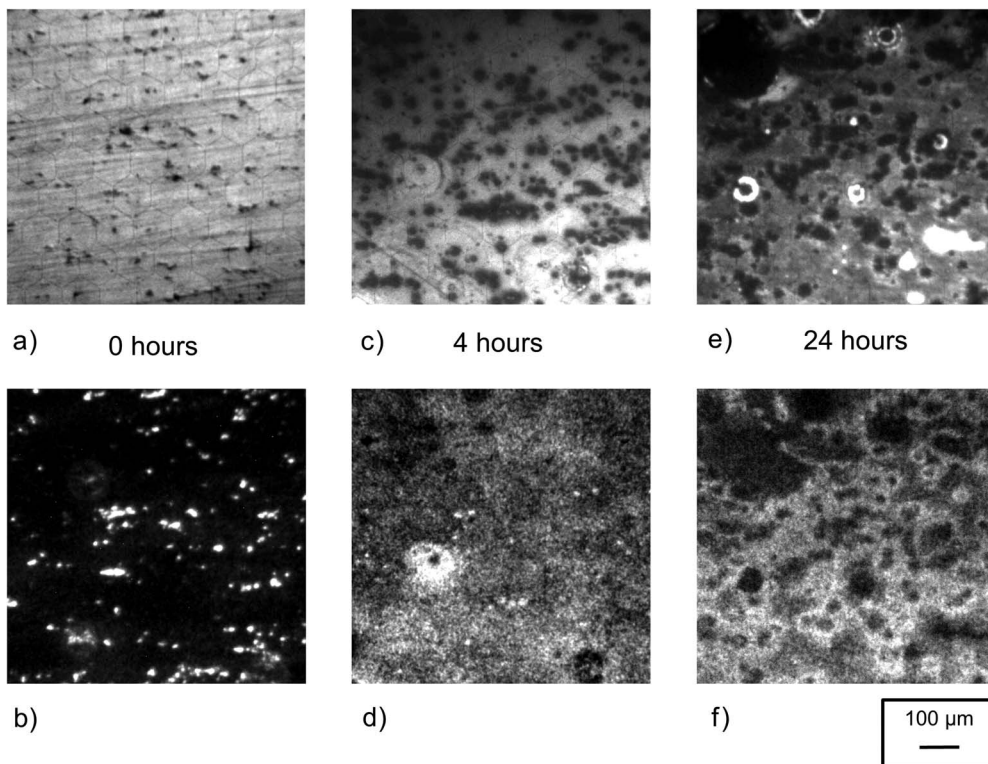


**Figure 16.** Surface appearance of the AA2024-T351 cube face center under tungsten illumination after a.) 0 hours, c.) 4 hours and e.) 24 hours of immersion in 0.51 M NaCl. The corresponding normalized ECL images are shown in b, d and f respectively.

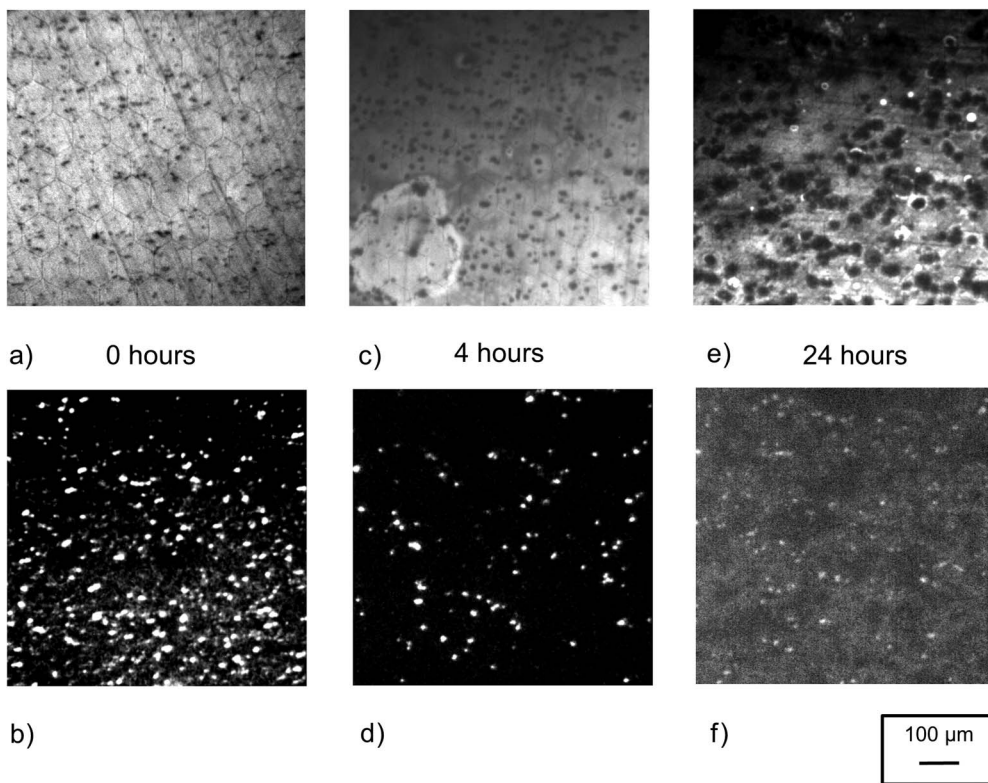


**Figure 17.** Surface appearance of the AA2024-T351 cube face edge under tungsten illumination after a.) 0 hours, c.) 4 hours and e.) 24 hours of immersion in 0.51 M NaCl. The corresponding normalized ECL images are shown in b, d and f respectively.

number of bright spots corresponding to IMPs, although the number density is lower than in Figure 17b. After 24 hours corrosion in aqueous NaCl the reflected light image of the sample surface Figure 17e shows further coarsening of the dark spots associated with the IMPs. However, in contrast to Figure 16f, the corresponding ECL image in Figure 17f still shows evidence of ECL light emission from the original IMP centers. Figure 17f also shows a general ECL emission from the matrix. A comparison of Figure 16c with 17c and Figure 16f with Figure 17f would suggest that IMP de-alloying and the re-distribution of electrochemically active Cu from those IMPs to the surrounding matrix occurs more quickly for IMPs located near the center line of the cube face sample (an area of net anodic activity in Figure 3) than for IMPs located near the sample edge (an area of net cathodic activity in Figure 3).

## Discussion

**Influence of IMP Cu on pit locations.**—A comparison of Figure 3 and Figure 6 show that the number density of stable corrosion pits evolving on the AA2024-T351 cube face sample is inversely dependent on the surface coverage by Cu rich IMPs  $[Cu_{IMP}]$ . That is to say that the highest number density of stable corrosion pits in Figure 6 occurs at, or near, the sample center-line which coincides with the minimum  $[Cu_{IMP}]$  in Figure 3. On this basis it seems unlikely that the probability of a stable pit evolving at a given location is determined by the number density of microscopic nucleation sites produced by, for example, S phase de-alloying at, or near, that location. The establishment of stable pits on AA2024 has previously been shown to occur immediately adjacent to S phase particles.<sup>4,28,29</sup> It has also been proposed that the alkalinity developed at the cathodic IMPs can dissolve the adjacent matrix giving rise to the appearance of grooves and pit-like clusters<sup>1,7,29-31</sup> which could later switch to an acidic pitting mechanism.<sup>7</sup> However, it is uncertain how cavity pH would change from alkaline to acidic without matrix re-passivation occurring at neutral values. Furthermore, the total pit densities reported for the phenomena observed were greater than typically measured for populations of stable pits, and it is likely that these were, in fact, transient events.<sup>7</sup>

Instead, it seems likely that the probability of pit stabilization is determined by the macroscopic distribution of ORR activity which is, in turn, determined by the macroscopic distribution of electrochemically active Cu. Furthermore, it seems reasonable to propose that the mechanism by which pit stabilization is directed away from regions of high ORR activity would involve local changes in electrolyte composition, and particularly increased pH, produced by the ORR. Thus, in those regions where coverage with electrochemically active Cu is high, cathodic current densities due to ORR are also high and solution alkalization will occur. High solution pH will tend to disfavor pit stabilization by making it more difficult to establish the required (acidic) pit electrolyte.

It is also evident from Figure 6 that the macroscopic distribution of local anodic and cathodic current density ( $j_z$ ) values does not change significantly over the 24 hour experimental period. That is to say, that whilst the anodic  $j_z$  peaks associated with individual stable corrosion pits may increase or decrease in magnitude over time, or even cease to exist if a pit re-passivates, there is no obvious change in the spatial distribution of stable pits over the corroding surface. There is, for example, no evidence to suggest that areas initially rich in anodic pits switch polarity over time to become intense net cathodes. This in marked contrast to results previously reported on commercially pure Mg (containing 600 ppm Fe) corroding in aqueous chloride electrolyte.<sup>49</sup> In the case of the magnesium a cathodic activation phenomenon associated with surface accumulation of Fe caused areas, which were initially anodic, to switch polarity and become intense cathode sites as corrosion proceeded.<sup>49</sup> The implication here is that, in the case of AA2024, any local increase in electrocatalytic activity for the ORR, resulting from corrosion-driven re-distribution of electrochemically active Cu, must be occurring in such a way as to conserve the original location of net anodic and cathodic activity, at least on the length scale that SVET can resolve (here distances greater than  $\sim 200 \mu\text{m}$ )

**ECL imaging.**—It may be understood from Figure 10 that under the experimental conditions used for ECL imaging (anodic pulse  $V_{max} = 0.8 \text{ V vs. SCE}$ ), effectively all the ECL light emitted from a Cu/Al mosaic surface will be emitted from areas of Cu. The reasons for this marked difference in ECL efficiency are not fully known but most probably arise from differences in the electrocatalytic activity of the metal (or metal oxide) surfaces. The  $V_{max}$  value of 0.8 V vs. SCE gives good sensitivity (high  $I_p$ ) without making the  $I_{ECL}$  vs. time response peak so narrow (Figure 8) as to cause difficulties in gating the camera exposure to capture the ECL image. Nevertheless, ECL imaging was only made practically useful when background luminol CL was suppressed by EDTA as shown in Figure 9.

Figure 9 shows that the  $I_p$  is reduced by around 20% as [EDTA] is increased from 0 to  $100 \times 10^{-6} \text{ M}$  whilst the background CL intensity is reduced by 98% when [EDTA] exceeds  $30 \times 10^{-6} \text{ M}$ . The background CL is emitted as a result of the ability of divalent transition metal cations, for example  $\text{Cu}^{2+}$ ,  $\text{Fe}^{2+}$ ,  $\text{Co}^{2+}$  and  $\text{Mn}^{2+}$ , to catalyse luminol ECL in aqueous solutions containing  $\text{O}_2$  and/ or  $\text{H}_2\text{O}_2$ .<sup>13,20-22</sup> It has been suggested that catalysis occurs via a Fenton type reaction (Equation 7).<sup>21</sup>



EDTA, amongst other chelating agents, reduces the ability of these cations to catalyse luminol ECL.<sup>21,22</sup> It is therefore probable that the background intensity recorded in the absence of EDTA, is a result of catalysis by transition metals present within reagents and water, or that have leached out from apparatus or glassware. It is subsequently suggested that the decrease in background ECL intensity, when EDTA is added, results from complexation and deactivation of metal cations. A value of  $5.25 \times 10^{-5} \text{ M}$  EDTA was chosen and was considered to be one at which the background light intensity was substantially reduced whilst ensuring that the reduction in  $I_p$  from the Cu electrode was not significant.

**Corrosion driven Cu re-distribution.**—Figure 16 shows that near the sample center line (area of net anodic activity) re-distribution of electrochemically active Cu occurs relatively quickly over a microstructural length scale (microns). The disappearance of the IMP centers, as sources of ECL light emission, and the appearance of ECL halos on the matrix surrounding the original IMP location is consistent with Cu re-distribution occurring (shown schematically in Figure 18a). The exact mechanism remains unclear but it seems reasonable to propose that re-distribution occurs through a combination of Cu 'cluster' re-deposition and  $\text{Cu}^{2+}$  ion re-plating (as outlined in the introduction to the current paper).<sup>1</sup> The ability to image the re-distributed Cu, using ECL, confirms that this Cu is electrically connected to the substrate. In previously published work of the behavior of a synthetic alloy (which consisted of photolithographically deposited  $1.8 \mu\text{m}$  diameter Cu discs separated by a distance ( $s$ ) of  $9.5 \mu\text{m}$ ) was compared with 2024-T3.<sup>64</sup> The results of this study caused the authors to conclude that matrix de-alloying and dissolution/back-plating contribute about equally to the Cu re-distribution process during corrosion of Al alloy 2024-T3 in 0.5 M NaCl.<sup>64</sup>

A contribution from matrix de-alloying in the region immediately proximal to cathodic IMPs (cathodic trenching) cannot be ruled out. However, the predominance of anodic activity near the sample center line implies that local electrolyte pH is more likely to be  $< \text{pH } 7$  than  $> \text{pH } 7$ .<sup>65</sup>

In contrast to Figure 16, Figure 17 shows that far from the sample center line (an area of net cathodic activity), re-distribution of electrochemically active Cu occurs more slowly. The IMP centers remain as sources of ECL light emission throughout the 24 hour experimental period. It would therefore appear likely that high local pH, resulting from ORR cathodic current, tends to retard the kinetics of IMP de-alloying and Cu re-distribution.  $\text{Mg}^{2+}$  is insoluble at high pH and the precipitated  $\text{Mg}(\text{OH})_2$  (solubility product  $K_{sp} = 1.8 \times 10^{-11} \text{ mol}^3 \cdot \text{dm}^{-9}$ )<sup>66</sup> would tend to protect against S phase de-alloying. It is also possible that the growth in ECL intensity seen in Figure 17 is the result of matrix de-alloying produced through matrix de-passivation and Al

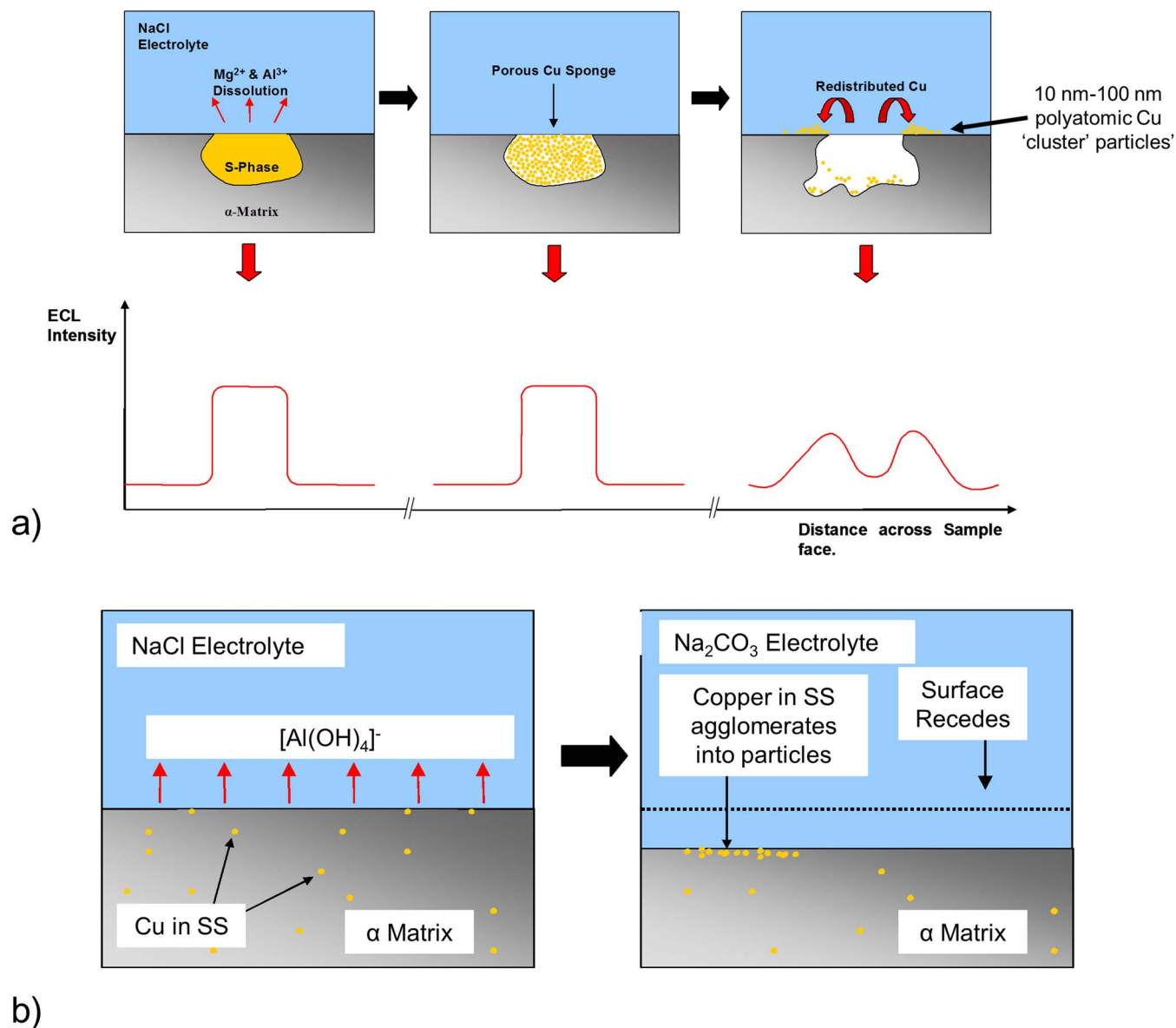


**Figure 18.** Schematics showing a.) the re-distribution of electrochemically active Cu over a microstructural length scale and b.) matrix de-alloying produced through matrix de-passivation at higher pH.

dissolution (Equation 1)<sup>22,24-27</sup> at higher pH. The receding matrix surface will expose Cu atoms held in solid solution (0.2-0.5 wt% Cu),<sup>25</sup> which can then agglomerate at the matrix surface as shown schematically in Figure 18b. Similarly, matrix dissolution could result in the exposure of Cu held in GP zones and dispersoids. We are unable to distinguish between these possibilities as these microscopic features cannot be resolved by the optical techniques used here. However, this notion is consistent with Figure 13 which shows the ECL emission pattern obtained after 4 hours of immersion in 0.1 M  $Na_2CO_3$  at pH 12. On this basis it seems reasonable to propose that the increased ECL emission from the center of the cube face (in Figure 13) results from solid solution Cu becoming exposed through Al dissolution rather than Cu becoming re-distributed from de-alloyed IMPs.

Figure 11 shows that one consequence of the corrosion driven microscopic (microns) re-distribution of electrochemically active Cu (seen in Figures 16 and 17) is to produce a change in the texture of the macro ECL image. That is to say, the re-distribution of Cu, away from IMP centers, to the surrounding matrix reduces the graininess or speckling of the macro ECL image. However, it is also evident that the distribution of electrochemically active Cu does not change

significantly over a macroscopic (mm) length scale. ECL emission intensity remains minimal near the sample center line and maximal furthest away from the center line. This finding implies that, whatever the exact mechanism of Cu re-distribution, it only occurs efficiently over distances  $\ll 1$  mm.

Comparison of Figure 6 and Figure 11 shows that the distribution of  $j_{z(x,y)}$  values follows the macroscopic distribution of electrochemically active Cu throughout the 24 hour experimental period of immersion in 0.51 M NaCl. This implies that changes in Cu distribution over a microstructural length scale have a minimal effect on the distribution of ORR activity, at least as far as this can be measured using SVET. Previously published work has concluded that the inhomogeneity caused by Cu-rich sites, both on 'synthetic' AA2024<sup>64</sup> and AA2024-T3,<sup>67</sup> does not strongly influence mass-transfer-limited ORR current in the case that IMP spacing ( $s$ ) is less than the Nernst diffusion layer thickness ( $\delta$ ). Under quiescent (unstirred) conditions, the value of  $\delta$  will typically be greater than the values of  $s$  in our samples (10 -100 micron). Computer simulations have also shown that changing  $s$  is not predicted to significantly influence the mass-transfer-limited current when  $\delta > s$ .<sup>67</sup> These results are consistent with the notion that changes

in Cu distribution over a microstructural length scale will have a minimal effect on the distribution of ORR activity, at least as this can be measured using SVET.

The AA2024-T351 cube sample used in the current paper has been intentionally processed to produce an inhomogeneous distribution of IMPs which is not normally the case in structural AA2024-T3 components. Nevertheless, it seems reasonable to assume that the action of Cu-rich IMPs in directing anodic attack, and the consequences of electrochemically active Cu re-distribution, would be broadly similar in both materials.

### Conclusions

An SVET and ECL imaging study was completed to investigate the corrosion-driven re-distribution of electrochemically active Cu which occurs during the free corrosion of AA2024-T351 in 0.51 mol dm<sup>-3</sup> aqueous NaCl.

- SVET was used to show that macroscopic (mm length scale) distribution of Cu containing intermetallic particles ([Cu<sub>IMP</sub>]) determined the location of net anodic or cathodic activity during corrosion. The highest number concentration of stable corrosion pits coincided with the lowest surface concentration of Cu-rich IMPs. Regions of net cathodic activity (oxygen reduction reaction ORR) coincided with the highest [Cu<sub>IMP</sub>].

- SVET also showed that the distribution of net anodic and net cathodic activity did not change appreciably over a 24 hour period of corrosion. Although the anodic current associated with individual corrosion pits might change over time the overall distribution of active pits on the sample surface did not. Thus, any corrosion-driven re-distribution of electrochemically active Cu did not appreciably effect the localization of corrosive attack (at least as far as this can be resolved by SVET).

- Macroscopic ECL imaging of electrochemically active Cu showed that initially (for un-corroded samples) electrochemically active Cu was primarily associated with Cu-containing intermetallic particles. Thus, regions of highest ECL light emission coincided with highest [Cu<sub>IMP</sub>]. Furthermore, imaging of corroded samples showed that the macroscopic distribution of electroactive Cu did not change significantly for corrosion periods of corrosion of up to 24 hours.

Microscopic ECL imaging (1-100 μm length scale) again showed that, initially, electrochemically active Cu was associated with IMPs. It also showed that as corrosion proceeded electrochemically active Cu became re-distributed from the IMPs to the surrounding matrix. This corrosion-driven re-distribution occurs more rapidly in regions of net anodic activity (low electrolyte pH) and more slowly in regions of net cathodic (ORR) activity (high electrolyte pH)

On the basis of these findings it is proposed that;

- In the highly conductive NaCl electrolyte used here the transition from transient to stable pitting, and therefore the location of stable pits on AA2024-T351, is determined chemically by local electrolyte pH, rather than by ohmic considerations.

- Electrochemically active Cu (associated with IMPs or otherwise) has the effect of directing pitting attack away from areas with a high surface coverage (of electrochemically active Cu). The probable mechanism by which this occurs involves the high local electrolyte pH produced by the ORR and the effect this has in reducing the probability that the pH within a transient pit will fall low enough to allow pit stabilization.

- The corrosion-driven re-distribution of electrochemically active Cu occurs efficiently over a microscopic length scale but not over a macroscopic length scale. This implies that the mechanisms of re-distribution, whether these involve the de-alloying IMPs, Cu ion replating, or matrix dissolution (cathodic trenching) only operate efficiently over a length scale similar to the dimensions on (or spacing between) the original IMPs.

- The corrosion-driven re-distribution of electrochemically active Cu over a microscopic length scale has minimal effect on the overall

rate or localization of corrosive attack in quiescent (unstirred) electrolyte because, under these conditions, the spacing between areas of electrochemically active Cu deposits is at all times less than the Nerst diffusion layer thickness. It may be understood that this circumstance might change under highly convected conditions when the diffusion layer thickness would be reduced.

### Acknowledgments

The authors would like to thank EPSRC, and BAE Systems for funding this work.

### ORCID

N. Wint  <https://orcid.org/0000-0002-9229-5728>

### References

- R. G. Buchheit, R. P. Grant, P. H. Hlava, B. Mckenzie, and G. L. Zender, *Journal of the Electrochemical Society*, **144**, 2621 (1997).
- V. Guillaumin and G. Mankowski, *Corrosion Science*, **41**, 421 (1999).
- I. J. Polmear, *Light Alloys - Metallurgy of the Light Metals*, Arnold, London (1995).
- P. Leblanc and G. S. Frankel, *Journal of the Electrochemical Society*, **149**, B239 (2002).
- R. Ambat and E. S. Dwarakadasa, *Journal of Applied Electrochemistry*, **24**, 911 (1994).
- C. Blanc, B. Lavelle, and G. Mankowski, *Corrosion Science*, **39**, 495 (1997).
- J. O. Park, C.-H. Paik, and R. C. Alkire, *Journal of the Electrochemical Society*, **143**, L174 (1996).
- T. J. Warner, M. P. Schmidt, F. Sommer, and D. Bellot, *Z. Metallkd.*, **86**, 494 (1995).
- K. Sugimoto, K. Hoshino, M. Kageyama, S. Kageyama, and Y. Sawada, *Corrosion Science*, **15**, 709 (1975).
- K. Urishino and K. K. Sugimoto, *Corrosion Science*, **19**, 225 (1979).
- G. O. Ilevbare, O. Schneider, R. G. Kelly, and J. R. Scully, *Journal of the Electrochemical Society*, **151**, B453 (2004).
- R. G. Buchheit, M. A. Martinez, and L. P. Montes, *Journal of the Electrochemical Society*, **147**, 119 (2000).
- G. S. Chen, M. Gao, and R. P. Wei, *Corrosion*, **52**, 8 (1996).
- J. R. Galvane and S. M. DeMicheli, *Corrosion Science*, **10**, 795 (1970).
- L. Muller and J. R. Galvele, *Corrosion Science*, **17**, 179 (1977).
- Y. V. Murty, T. Z. Kattamis, and O. Devereux, *Corrosion (Houston)*, **31**, 207 (1975).
- R. G. Buchheit, *Journal of the Electrochemical Society*, **142**, 3994 (1995).
- R. Parvizi, A. E. Hughes, and M. Forsyth, *Corrosion Reviews*, **33**, 1 (2015).
- W. W. Binger, E. H. Hollingsworth, and D. O. Sprowls, *Aluminum, Vol. I: Properties, Physical Metallurgy, and Phase Diagrams*, American Society for Metals (1967).
- M. J. Prior and J. C. Foster, *Journal of the Electrochemical Society*, **131**, 1230 (1984).
- R. G. Buchheit, L. M. Maestas, and N. R. Sorensen, *Corrosion Protection by Coatings and Surface Modification*, Pennington, NJ (1993).
- M. B. Vukmirovic, N. Dimitrov, and K. Sieradzki, *Journal of the Electrochemical Society*, **149**, B428 (2002).
- N. Dimitrov, J. A. Mann, M. Vukmirovic, and K. Sieradzki, *Journal of the Electrochemical Society*, **147**, 3283 (2000).
- T. R. Leclere and R. C. Newman, *Journal of the Electrochemical Society*, **149**, B52 (2002).
- L. F. Monodolfo, *Aluminium Alloys: Structure and Properties*, Butterworth Markam (1976).
- H. H. Uhlig, *The Corrosion Handbook*, John Wiley (1948).
- P. Hulser, U. A. Kruger, and F. Beck, *Corrosion Science*, **38**, 47 (1996).
- K. Nisanciolu and H. Holtan, *Corrosion Science*, **19**, 537 (1979).
- Y. Zhu and G. S. Frankel, *Corrosion*, **75**, 29 (2019).
- R. P. Wei, C.-M. Liao, and R. O. C. Ming, *Metallurgical and Materials Transactions A*, **29A**, 1153 (1998).
- K. Shimizu, K. Kobayashi, G. E. Thompson, and G. C. Wood, *Corrosion Science*, **34**, 1475 (1993).
- A. J. Aldykewicz, H. S. Isaacs, and A. J. Davenport, *Journal of the Electrochemical Society*, **142**, 3342 (1995).
- N. Harvey, *Journal of Physical Chemistry*, **33**, 1456 (1929).
- J. E. Vitt, D. C. Johnson, and R. C. Engstrom, *Journal of the Electrochemical Society*, **138**, 1637 (1991).
- K. E. Haapakka and J. J. Kankare, *Analytica Chimica Acta*, **138**, 263 (1982).
- G. Merenyi and J. S. Lind, *American Chemistry Society*, **102**, 5830 (1980).
- J. Lind, G. Merenyi, and T. E. Eriksen, *Journal of the American Chemical Society*, **105**, 7655 (1983).
- B. Epstein and T. Kuwana, *Journal of Electroanalytical Chemistry*, **15**, 389 (1967).
- B. Epstein and T. Kuwana, *Photochemistry and Photobiology*, **6**, 605 (1967).
- G. P. Jirka, A. F. Martin, and T. A. Nieman, *Analytica Chimica Acta*, **284**, 345 (1993).
- S. Sakura, *Analytica Chimica Acta*, **262**, 49 (1992).
- N. N. Rozhitskii, *Journal of Analytical Chemistry*, **47**, 1288 (1992).
- L. J. Kricka, X. Ji, G. H. G. Thorpe, B. Edwards, J. Voyta, and I. Bronstein, *Journal of Immunoassay*, **17**, 67 (1996).

44. O. M. Huta, B. Y. Heneha, O. M. Romaniv, V. O. Vasylechko, and S. V. Midyani, *Materials Science*, **31**, 307 (1995).
45. L. L. Klopff and T. A. Nieman, *Analytical Chemistry*, **55**, 1080 (1983).
46. D. Zhu and W. J. van Ooij, *Corrosion Science*, **45**, 2163 (2003).
47. X. Zhang, T. Hashimoto, J. Lindsay, and Z. Zhou, *Corrosion Science*, **108**, 85 (2016).
48. T. Hashimoto and G. E. Thompson, *Corrosion Science*, **103**, 157 (2016).
49. G. Williams and H. N. McMurray, *J. Electrochem. Soc.*, **155**, C340 (2008).
50. S. Bohm, H. N. McMurray, S. M. Powell, and D. A. Worsley, *Electrochimica Acta*, **45**, 2165 (2000).
51. D. Worsley, H. N. McMurray, and A. Belghazi, *Chem. Commun.*, **24**, 2369 (1997).
52. S. M. Powell and D. A. Worsley, *British Corrosion Journal*, **36**, 42 (2001).
53. G. Williams, H. N. McMurray, and R. Grace, *Electrochimica Acta*, **55**, 7824 (2010).
54. H. S. Isaacs, *J. Electrochem. Soc.*, **138**, 722 (1991).
55. G. W. C. Kaye and T. H. Laby, *Tables of Physical and Chemical Constants*, p. 219, Longman, London (1986).
56. H. N. McMurray and B. P. Wilson, *Journal of Physical Chemistry A*, **103**, 3955 (1999).
57. I. Parejo, C. Petrakis, and P. Kefalas, *Journal of Pharmacological and Toxicological Methods*, **43**, 183 (2000).
58. T. G. Burdo and W. Rudolf, *Seitz, Analytical Chemistry*, **47**, 1639 (1975).
59. W. Chen, L. Hong, A. L. Liu, J. Q. Liu, X. H. Lin, and X. H. Xia, *Talanta*, **99**, 643 (2012).
60. T. Ariga, Y. Imura, M. Suzuki, and E. Yoshimura, *Journal of Chromatography B*, **1014**, 75 (2016).
61. A. Molina and E. Laborda, *Electrochimica Acta*, **286**, 374 (2018).
62. Z. Huda, I. Taib, and T. Zaharinie, *Materials Chemistry and Physics*, **113**, 515 (2009).
63. H. N. McMurray, D. Williams, and D. A. Worsley, *Journal of the Electrochemical Society*, **150**, B567 (2003).
64. M. B. Vukmirovic, N. Vasiljevic, N. Dimitrov, and K. Sieradzki, *Journal of the Electrochemical Society*, **150**, B10 (2003).
65. H. S. Isaacs, G. Adzic, and C. S. Jeffcoate, *Corrosion*, **56**, 971 (2000).
66. L. G. Sillén, A. E. Martell, and J. Bjerrum, *Stability Constants of Metal-Ion Complexes*, The Chemical Society, London (1964).
67. M. A. Jakab, D. A. Little, and J. R. Skully, *Journal of the Electrochemical Society*, **152**, B311 (2005).